small

Lithium-Ion Batteries

Solvothermal-Induced Self-Assembly of Fe_2O_3/GS Aerogels for High Li-Storage and Excellent Stability

Ronghua Wang, Chaohe Xu, Meng Du, Jing Sun, Lian Gao,* Peng Zhang, Heliang Yao, and Chucheng Lin*

***We** develop a novel solvothermal-induced self-assembly approach, using colloid sol as precursor, to construct monolithic 3D metal oxide/GS (graphene sheets) aerogels. During the solvothermal process, graphene oxide (GO) is highly reduced to GS and self-assembles into 3D macroscopic hydrogels, accompanying with in situ transformation of colloid sol to metal oxides. As a proof of concept, Fe_2O_3/GS aerogels are synthesized based on $Fe(OH)_3$ sol, in which GS self-assemble into an interconnected macroporous framework and Fe_2O_3 nanocrystals (20–50 nm) uniformly deposit on GS. Benefitting from the integration of macroporous structures, large surface area, high electrical conductivity, and good electrode homogeneity, the hybrid electrode manifests a superior rate capability (930, 660 and 520 mAh g^{-1} at 500, 2000 and 4000 mA g^{-1}, respectively) and excellent prolonged cycling stability at high rates (733 mAh g^{-1} during 1000 charge/discharge cycles at 2000 mA g^{-1}), demonstrating its great potential for application in high performance lithium ion batteries. The work described here provides a versatile pathway to construct various graphene-based hybrid aerogels.*

1. Introduction

Lithium ion batteries (LIBs), with high energy density, high voltage, and environmental friendliness, are the crucial supplements in energy storage devices that can meet continuous energy demands and environmental concerns.[1–3] In order to satisfy the increasing demand for higher reversible capacities, nanostructured metal oxides, such as SnO_2,[4] Fe_2O_3[5], Fe_3O_4,[6,7] Co_3O_4[2] and TiO_2,[8] have been regarded as potential anode materials for LIBs and widely studied for their higher reversible capacities than commercial graphite (372 mAh g^{-1}). Unfortunately, their practical application still suffers from the large volume expansion and agglomeration during lithium alloying/de-alloying process, resulting in pulverization, electrical connectivity loss and finally rapid capacity fading of electrodes.[9] Besides, the insulating property of metal oxide further limits electrochemical reaction kinetics. To circumvent these issues, various strategies have been developed to improve the structural integrity and electrical conductivity by optimizing particle sizes,[10] designing novel nanostructures[11,12] and fabricating metal oxide/carbon hybrids.[13,14]

Graphene sheets (GS), with large specific surface area, high electrical conductivity, and extraordinary mechanical properties, can serve as an intriguing substrate to anchor electrochemically active materials and accommodate their volume change during cycling.[6,15] Hence, various graphene-based hybrids have been developed with improved lithium storage.[3,16,17] However, most of the previous works focused

R. H. Wang, C. H. Xu, M. Du, Prof. J. Sun, Prof. L. Gao, H. L. Yao, C. C. Lin
The State Key Lab of High Performance Ceramics and Superfine Microstructure
Shanghai Institute of Ceramics
Chinese Academy of Sciences
Shanghai 200050, P. R. China
E-mail: jingsun@mail.sic.ac.cn; liangao@mail.sic.ac.cn
Prof. L. Gao, P. Zhang
State Key Laboratory for Metallic Matrix Composite Materials
School of Materials Science and Engineering
Shanghai Jiao Tong University
Shanghai 200240, P. R. China

DOI: 10.1002/smll.201303371

on the preparation of two-dimensional (2D) graphene-based composites, in which nanoparticles anchored on the surface of GS. Recently, it has been revealed that the assembly of 2D GS into macroscopic 3D architectures can provide resultant graphene-based composites with large specific surface area and fast electron transport kinetics due to the 3D interconnected framework combined with intriguing properties of graphene.[18,19] Chen et al. have pioneered the capture of pre-prepared Fe_3O_4 into 3D graphene network by a mild chemical reduction (~90 °C without stirring) with the aids of reducing agents ($NaHSO_3$, Na_2S, vitamin C, HI, and hydroquinone).[20,21] Despite the mild condition, a large amount of reducing agents have to be provided to satisfy the reduction of GO and self-assembly. Graphene-based hydrogels were also constructed based on hydrothermal treatment under high pressure, during which GO/metal salts[19,22–24] or GO/pre-prepared metal oxide[25–27] self-assembled together into hydrogels accompanied with hydrothermal reduction of GO to GS. Benefitting from the unique architecture, these graphene-based hydrogels showed great potentials in a broad range of LIBs, electrochemical capacitors, water treatment, catalysis and so on. In the field of energy storage, although the great improvement has been achieved on electrochemical performance, some disadvantages for lithium storage still exist in these hybrids, such as inferior interfacial contact between GS and pre-prepared metal oxide,[20,26] relative large particle size[19,25] (>100 nm) and serious aggregation[19,20,24,26,28] when metal salts were used as precursor. Consequently, the cycle life (typically <100 cycles) is still unsatisfactory for practical applications.

Herein, we report a new solvothermal-induced self-assembly approach, using colloid sol as precursor, to construct monolithic 3D metal oxide/GS aerogels, aiming at enhancing the lithium-storage performance, especially the cyclic performance. Unlike the commonly used metal salts precursors (hard to control with proceeding of reaction), colloid sol, with uniform size and excellent dispersibility, can ensure the final nanoparticles a small size and even distribution. Compared with the general hydrothermal treatment, solvothermal treatment can further restrict the coarsening of resulted nanocrystals, enable a more thorough reduction of GS, and endow the composite a higher electrical conductivity. As a proof of concept, $Fe(OH)_3$ sol was chosen as a model framework due to its ease of fabrication and the highest theoretical capacity of Fe_2O_3 (1005 mAh g^{-1}) among metal oxide.[3,29] The resultant Fe_2O_3/GS aerogels, with uniform deposition of Fe_2O_3 of 20–50 nm, possess the key factors for high performance electrode: macroporous structures, large surface area, high electrical conductivity, and good electrode homogeneity. Our results confirmed the effectiveness of this solvothermal-induced self-assembly approach to the final performance of the electrode, especially its long-term cycle stability. As a result, the Fe_2O_3/GS electrode delivered a high capacity of 733 mAh g^{-1} during 1000 charge/discharge cycles at 2000 mA g^{-1}, with a capacity decay as low as 0.027% per cycle. To the best of our knowledge, the lithium storage performances are among the highest values achieved in Fe_2O_3 based electrode materials. This work initiated a novel approach to construct 3D graphene-based composites, and the method is versatile for other metal oxide/GS hydrogels.

2. Results and Discussion

Figure 1 schematically demonstrates the experimental procedure. As is well known from colloidal science, hydroxide colloid and oxide colloid are typically positively charged due to the adsorption of cations, while GO was negatively charged due to the presence of oxygen-containing groups. The electrostatic interaction between the positively charged colloid and

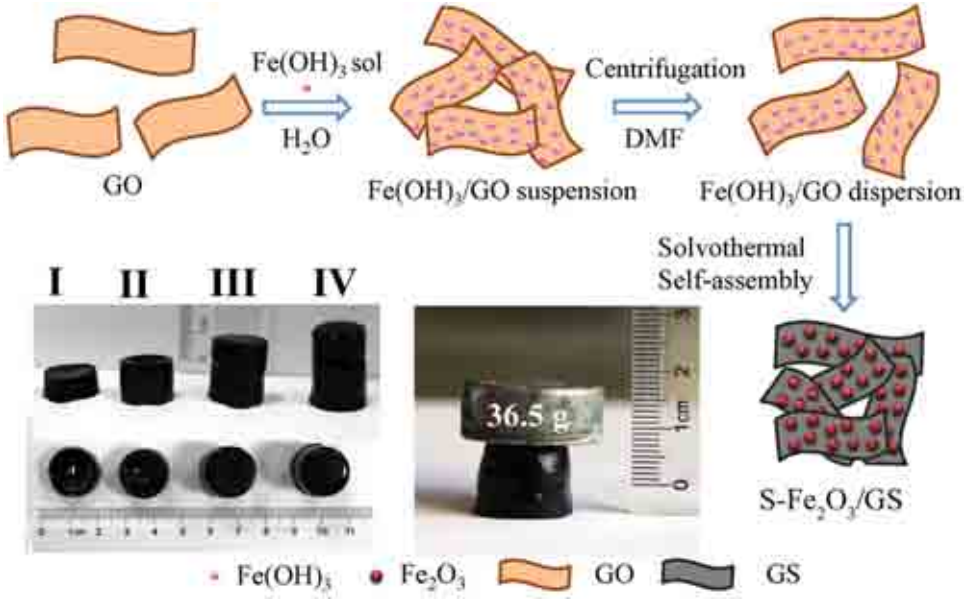

Figure 1. Schematic illustration of preparation of S-Fe_2O_3/GS aerogels. The left photograph is S-Fe_2O_3/GS hydrogels with increasing size, obtained by solvothermal treatment of 10 mL (I), 20 mL (II), 30 mL (III) and 40 mL (IV) $Fe(OH)_3$/GS dispersions. The right one shows the S-Fe_2O_3/GS supporting a 36.5 g iron plate.

small 2014,
DOI: 10.1002/smll.201303371

the negatively charged GO drives close combination between the two components upon mixing. In this case, the combination of $Fe(OH)_3$ (zeta potential of +129.8 mV) and GO (zeta potential of –61.8 mV) afforded a tight and uniform $Fe(OH)_3$ deposition on the surface of GO (see Supporting Information, Figure S1). During solvothermal treatment in DMF, GO was reduced to GS[30] accompanying with in situ transformation of $Fe(OH)_3$ to Fe_2O_3. Meanwhile, GS anchored with Fe_2O_3 nanoparticles acted as building blocks and self-assembled into 3D macroscopic hydrogels with an interconnected network. This process is driven by the π–π stacking interactions due to the decreased oxygenated groups on graphene.[28,31] Compared with the existing approaches for hydrogels fabrication, our solvothermal-induced self-assembly process offers several advantages. (i) DMF solvothermal reaction, a more effective reduction method that requires no additional reducing agents, could achieve a deeper reduction of GO than a general hydrothermal treatment, thus endowing the composite a higher electrical conductivity (277.5 and 31.8 S m^{-1} for S-Fe_2O_3/GS and H-Fe_2O_3/GS, respectively). (ii) $Fe(OH)_3$ sol has an ultra-small size and excellent dispersibility, which ensure a small size and uniform distribution for the final Fe_2O_3 nanoparticles. (iii) The strong electrostatic interaction drives an intimate contact between Fe_2O_3 and GS, which facilitates fast interfacial electron and ion transport. As shown in the left digital photograph (Figure 1), the size of hydrogels can be easily tailored by changing the volume of $Fe(OH)_3$/GS dispersions. The obtained hydrogels are mechanically strong enough to support a 36.5 g iron plate, showing a good robustness.

The XRD patterns reveal the peaks of Fe_2O_3 in S-Fe_2O_3/GS, which can be well indexed to JCPDF 33–0664 (Figure S2a). No diffraction peak corresponding to the restacking of GS to form graphite can be observed, suggesting the agglomeration of GS was effectively prevented. The graphene contents were measured to be 45.9% and 47.2% for S-Fe_2O_3/GS and H-Fe_2O_3/GS, respectively (Figure S2b) using TG analysis.

The morphology and microstructure of the as-prepared S-Fe_2O_3/GS were investigated by SEM and TEM (**Figure 2**). SEM image reveals a well-defined and interconnected 3D porous graphene network with macropores in the micrometer size range (Figure 2a). All of the GS are covered by the Fe_2O_3 nanocrystals with a particle size of 20–50 nm (Figure 2b). The small size of Fe_2O_3 is able to partially buffer the stress and strain related to volume expansion/contraction and reduce the lithium ion transportation path.[32] TEM observations confirm the even distribution of Fe_2O_3 on GS (Figure 2c,d). The Fe_2O_3 particle in Figure 2e is highly crystallized with a lattice spacing of 0.27 nm, which can be assigned to the interspacing of the (104) planes. The corresponding SAED pattern further confirms the high-quality single-crystalline nature of Fe_2O_3. The layer number of GS was about 3~5, as displayed by HRTEM in Figure S3, indicating GS was highly exfoliated. The pure Fe_2O_3 sample, prepared under the same conditions without the addition of graphene, consisted of microspheres with a diameter of several micrometers (Figure S4). The magnified images show that the microspheres are composed of nanoparticles of ~100 nm, which is much larger than the 20–50 nm in S-Fe_2O_3/GS. Obviously, the presence of graphene played an important role in tailoring the crystal growth of Fe_2O_3.

To understand the mechanism of the self-assembly process, several control experiments were carried out. First, $Fe(OH)_3$/GO dispersion in H_2O was hydrothermally treated under the same conditions. However, this hydrothermal approach did not work well for the formation of 3D graphene framework and only a black powdery material was produced (inset in **Figure 3**c). Since π–π stacking interactions are the driving force of the self-assembly,[28,31] the reduction effect of GS plays a key role in determining whether hydrogels can form or not. Here, hydrothermal reduction is less effective in diminishing oxygenated functionalities and restoring the π-conjugated structures of GS.[30] This was proved by the XPS results: the C/O ratio of GS in H-Fe_2O_3/GS (4.74) was much lower than that in S-Fe_2O_3/GS (Figure 3a) (6.22, deducting oxygen from Fe_2O_3); moreover, a lower intensity of oxygen-containing groups in S-Fe_2O_3/GS was also observed in the corresponding C1s spectra (Figure 3b). As a result, the mild hydrothermal reduction resulted in a weak strength of π-π stacking and inadequate cross-linking sites for forming a 3D network.[31] SEM revealed that the dispersion of Fe_2O_3 in H-Fe_2O_3/GS was as homogeneous as that in S-Fe_2O_3/GS (Figure 3c and d). However, the particles are irregularly shaped, and much bigger (~80 nm) than those in S-Fe_2O_3/GS. This indicates the effect of solvothermal environment in restricting the growth of particles relative to hydrothermal treatment.

In another control experiment, when $Fe(OH)_3$ sol was replaced with metal salt $FeCl_3$ (the same salt for $Fe(OH)_3$ sol preparation), the solvothermal approach also worked well for the formation of 3D graphene framework (inset in Figure 3e), accompanying with successfully transformation of $FeCl_3$ to Fe_2O_3 (Figure S5). However, a layer of free Fe_2O_3 was visible on the top of hydrogels (the red area), indicating an inhomogeneous distribution of Fe_2O_3. TEM images show that the free Fe_2O_3 is composed of nanoflowers (Figure 3e and Figure S6), while those inside the hydrogel are nanoparticles agglomerated severely on the surface of GS (Figure 3f). To understand the difference between metal salts and colloidal sol, solvothermal reactions with different durations were carried out. For $FeCl_3$/GO-DMF, GS self-assembled into a hydrogel after 2 h, leaving a yellow solvent (**Figure 4**a). Adding the yellow solvent into NaOH will lead to the formation of reddish brown precipitate, indicating presence of $FeCl_3$ in DMF. It is also the case for $FeCl_3$-DMF after 2 h solvothermal reaction. This means the transformation from $FeCl_3$ to Fe_2O_3 was much slower than assembly of GS. During subsequent stage of solvothermal reaction, those un-reacted $FeCl_3$ tended to deposit on the surface of hydrogels and resulted in an inhomogeneous distribution. On the other hand, besides heterogeneous nucleation on the surface of GS, Fe^{3+} will also nucleate in solvent. The whole nucleating process was complicated and hard to control with proceeding of reaction, agglomeration of Fe_2O_3 was also prone to appear inside the hydrogel (Figure 3f). However, this is not the same case as $Fe(OH)_3$ sol, which possesses excellent dispersibility and has already been homogeneously anchored

DOI: 10.1002/smll.201303371

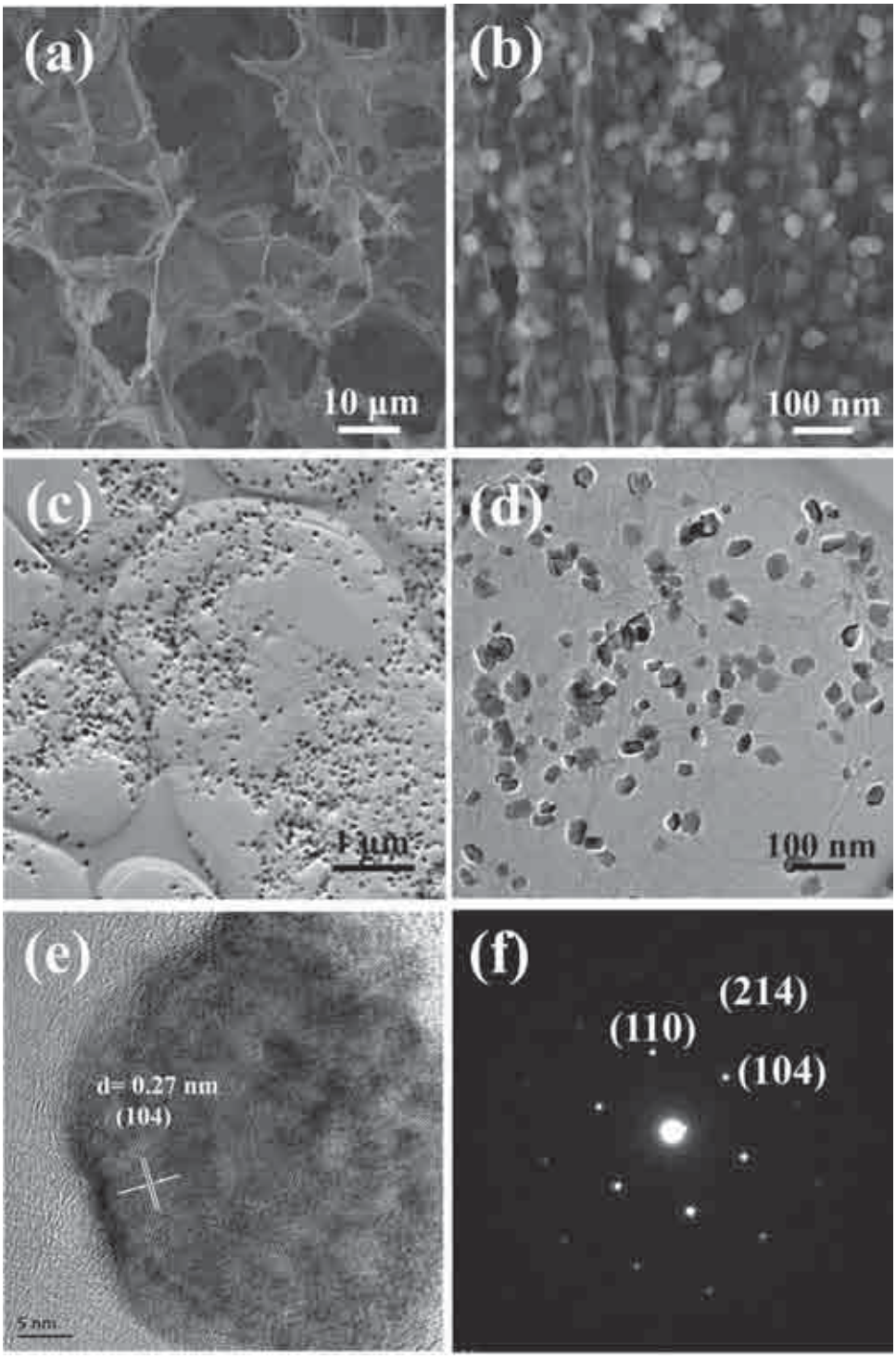

Figure 2. SEM (a-b), TEM (c-d) and HRTEM images (e) of S-Fe_2O_3/GS; (f) the corresponding SAED pattern.

on the surface of GO before reaction (Figure S1).[33] Upon reaction, $Fe(OH)_3$ nanoparticles were in situ transformed into Fe_2O_3, thus ensuring the final Fe_2O_3 nanoparticles an even distribution within the hybrid (Figure 4b). Based on the above discussion, we can conclude that it was the solvothermal treatment that restricts the growth of Fe_2O_3 particles, enables a more thorough reduction of GS, and induces the self-assembly process; the $Fe(OH)_3$ sol precursor ensures an excellent dispersibility for the final Fe_2O_3. Importantly, this solvothermal-induced self-assembly process is a versatile approach for fabrication of graphene/metal oxide hydrogels. Furthermore, the colloidal precursor is not limited to hydroxide colloid but can be extended to oxide colloid. For example, macroscopic SnO_2/GS hydrogels were also obtained when using SnO_2 sol as precursor (Figure S7).

The porous nature of S-Fe_2O_3/GS architecture was also characterized by BET measurement. The N_2 adsorption-desorption isotherms exhibited a typical IV hysteresis loop at a

DOI: 10.1002/smll.201303371

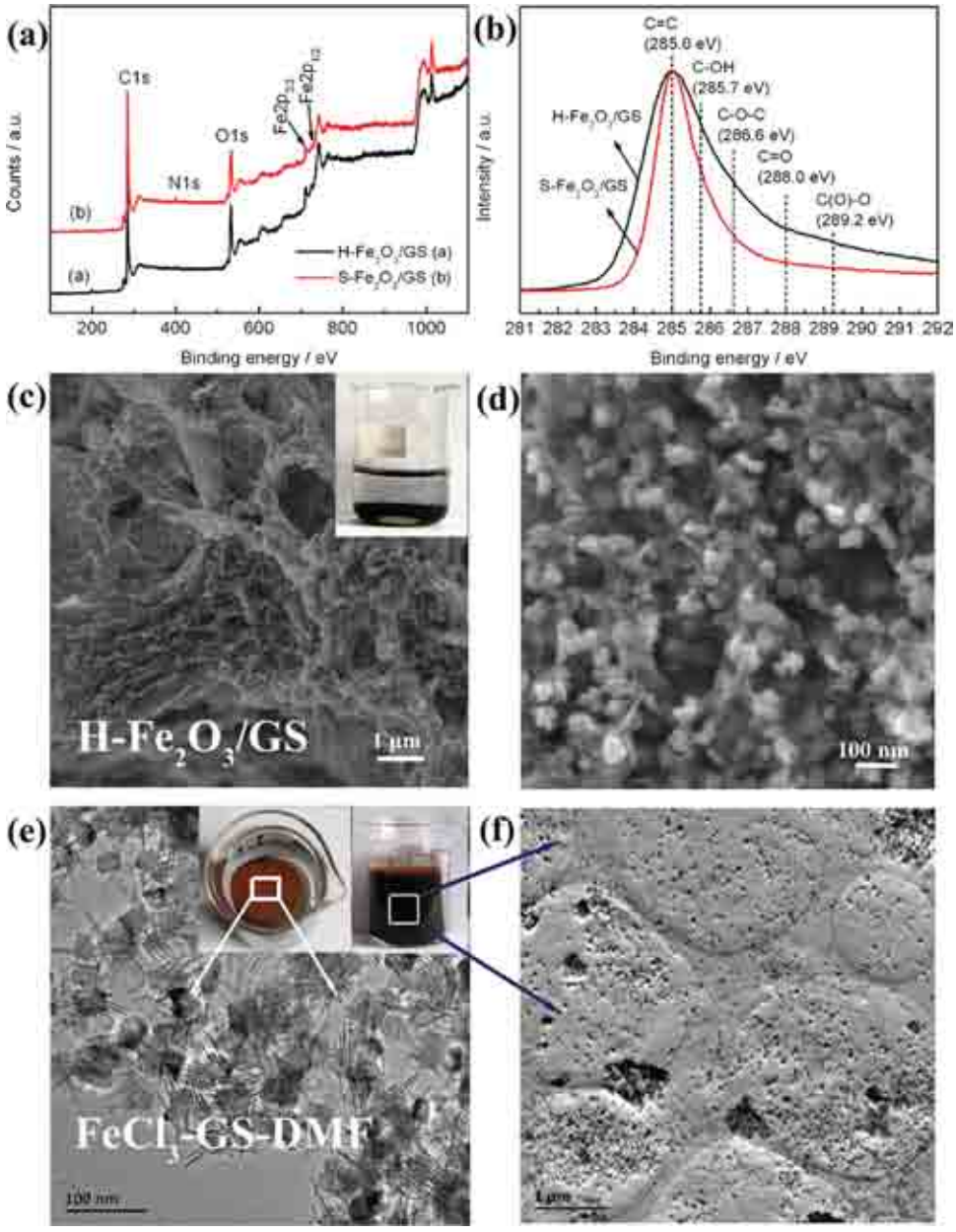

Figure 3. (a) XPS and (b) the C1s spectra of S-Fe_2O_3/GS and H-Fe_2O_3/GS; (c-d) SEM images of H-Fe_2O_3/GS, the inset in (c) is a digital photograph of H-Fe_2O_3/GS; (e) TEM image of Fe_2O_3 on the top of Fe_2O_3/GS hydrogels (the red area) when replacing $Fe(OH)_3$ sol with metal salt $FeCl_3$, the inset in (e) is the corresponding digital photographs from the top view (left) and side view (right); (f) TEM image of Fe_2O_3/GS inside the hydrogel (the dark area).

relative pressure between 0.4 and 0.9, characteristic of pores with different pore sizes (**Figure 5**). Remarkably, the specific surface area of S-Fe_2O_3/GS reached up to 212.1 $m^2\ g^{-1}$, which contrasted markedly to that of pure Fe_2O_3 (10.0 $m^2\ g^{-1}$). This result highlights the building up of 3D frameworks by solvothermal assembly is an effective way to achieve a high surface area for hybrid materials. BJH calculations disclose a pore volume of 0.15 $cm^3\ g^{-1}$ and an average pore diameter of 3.6 nm (the inset in Figure 5a). The high porosity can provide not only more surface reaction sites but also sufficient buffer space to alleviate the volume expansion of Fe_2O_3 during lithiation and delithiation, and is therefore favorable for the electrochemical properties.[23,34]

Coin cells with metallic Li counter electrode were assembled to evaluate the electrochemical performance of the electrode. Detailed discussions were carried out on the optimized sample with graphene content of 45.9% hereafter (Figure S8). **Figure 6**a displays the CV curves for the first five cycles of S-Fe_2O_3/GS electrode. In the first cycle, one cathodic peak at 0.74 V corresponded to the electrochemical reduction reaction of Fe_2O_3 and the formation of solid electrolyte interphase (SEI).[12] The anodic peak at 1.75 V can be attributed to the reversible oxidation of Fe^0 to Fe_2O_3.[35,36] The reversible reaction occurring with lithium can be described by the following electrochemical conversion reactions:

DOI: 10.1002/smll.201303371

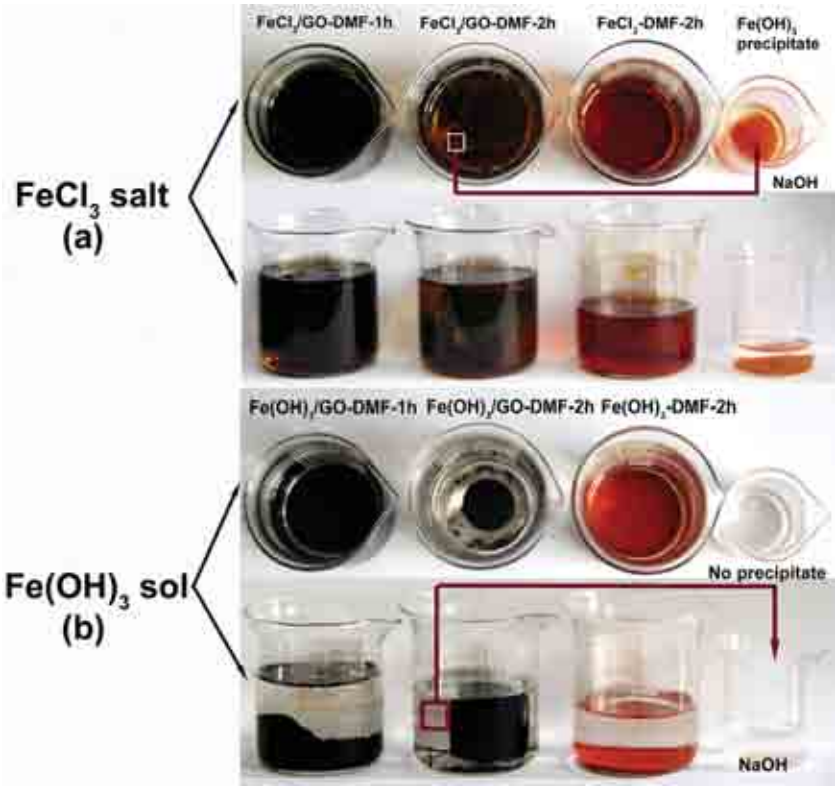

Figure 4. The photographs of Fe_2O_3/GS prepared by solvothermal reaction of $FeCl_3$/GO-DMF, $FeCl_3$-DMF, $Fe(OH)_3$/GO-DMF and $Fe(OH)_3$-DMF after different amounts of time. For both (a) and (b), the photographs were taken from the top and side view, respectively. Note that the hydrogels had formed for $FeCl_3$/GO-DMF-2h and $Fe(OH)_3$/GO-DMF-2h. However, they were partially broken during transfer process because of inadequate robustness.

$$Fe_2O_3 + 6Li^+ + 6e^- \leftrightarrow 2Fe + 3Li_2O \quad (1)$$

In the subsequent cycles, the main reduction peak shifted to ~0.76 V while the main anodic peak at ~1.75 V showed very little modification. The peak intensity and integral areas are nearly identical, suggesting the good reversibility of lithium insertion and extraction reactions.[6] In contrast, the peak intensity and integrated area for pure Fe_2O_3 dropped rapidly (Figure S9), indicating large capacity loss occurred in the lithium storage process.

Figure 6b shows the representative charge/discharge profiles of S-Fe_2O_3/GS at a current density of 100 mA g^{-1} between 0.01–3 V vs. Li^+/Li. A potential plateau appears at ~0.8 V during the first discharge process, which is in good agreement with the CV results. The initial charge and discharge capacities are 1340 and 2417 mAh g^{-1}, respectively, based on the total mass of composites. The lithium storage capacities were greatly higher than the theoretical capacity of Fe_2O_3 (1005 mAh g^{-1}) owing to the formation of SEI layer and possibly interfacial Li^+ storage.[14,37] From the 2nd to 10th cycles, although slightly decreased, the capacity can still reach up to 1250 mAh g^{-1}. The unique macroscopic 3D architectures, with high specific surface area and porous structure, should play an important role in delivering such high capacities. Additionally, the coulombic efficiency approached 100% from the second cycle, suggesting a facile lithium insertion/extraction associated with efficient transport of ions and electrons in the electrode.[38]

Figure 6c and d exhibit the rate performance of S-Fe_2O_3/GS, H-Fe_2O_3/GS and pure Fe_2O_3 at different current densities. For S-Fe_2O_3/GS, reversible capacities of 1300, 930, 790 and 660 mAh g^{-1} were realized at current densities of 100, 500, 1000 and 2000 mA g^{-1}, respectively, further demonstrating the high reversible capacity of the electrode. Even at very high current densities, such as 4000, 5000 and 6000 mA g^{-1}, the electrode still maintained a capacity of 520, 460 and 370 mAh g^{-1}, respectively, which are far exceeding the capacity of graphite at low current density (~350 mAh g^{-1}). Remarkably, the charge/discharge curves still maintain kinetics feature at high current densities (Figure 6d), indicating a facile charge transport process.[38] When the current density returned to 100 mA g^{-1}, a capacity of 1220 mAh g^{-1} was recovered in another 5 cycles. This

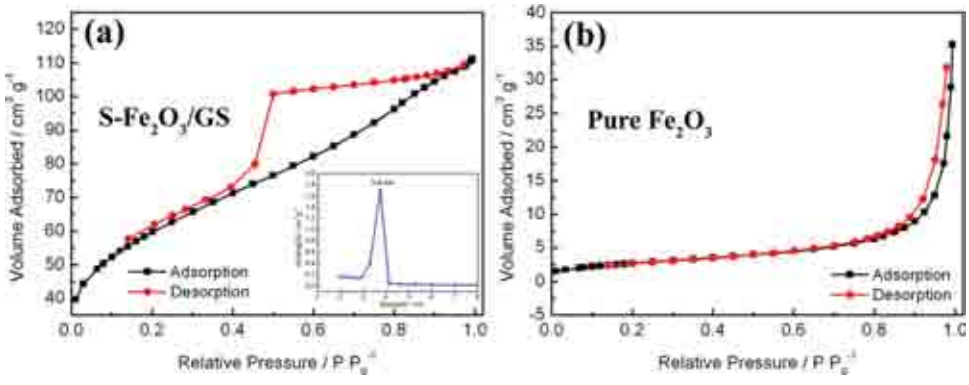

Figure 5. Nitrogen adsorption and desorption isotherms of S-Fe_2O_3/GS (a) and pure Fe_2O_3 (b).

small 2014,
DOI: 10.1002/smll.201303371

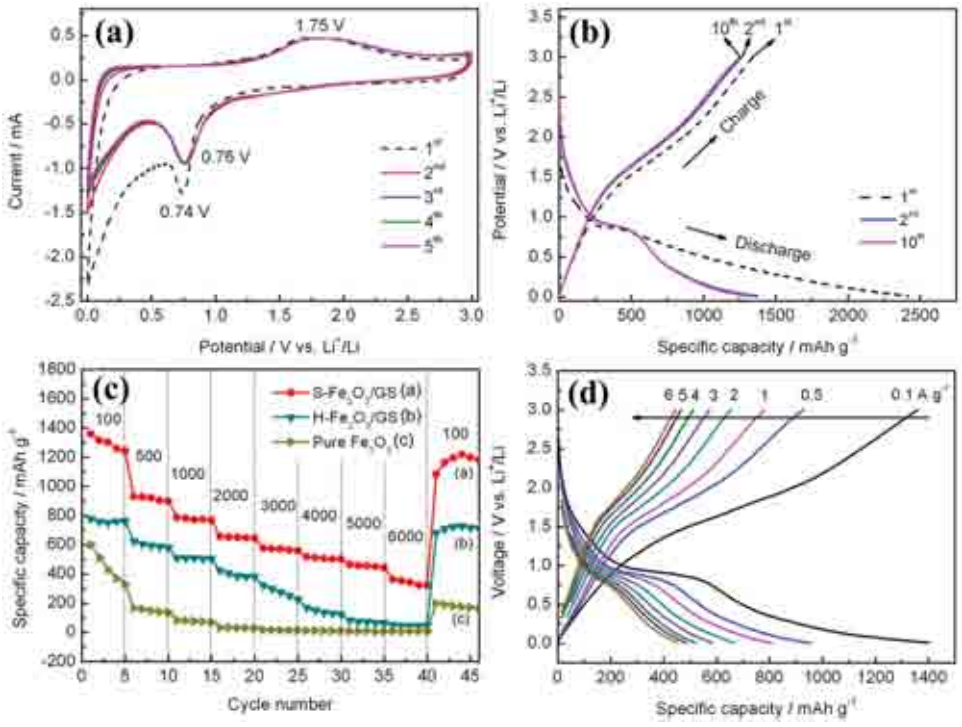

Figure 6. (a) Cyclic voltammograms for the first five cycles of S-Fe_2O_3/GS electrode; (b) charge-discharge voltage profiles of S-Fe_2O_3/GS electrode at a current density of 100 mA g^{-1}; (c) rate capability and (d) the corresponding charge/discharge curves of the electrode at different current densities (100–6000 mA g^{-1}).

further implied the stable structure of the electrode and good reversibility. Noteworthy, the rate capability of our S-Fe_2O_3/GS outperforms those of reported Fe_2O_3/GS aerogels (372 mAh g^{-1} under the current density of 5000 mA g^{-1})[19] and most of other Fe_2O_3 based hybrids[10,12,16,35,37,39] (few of them have reported the rate performance under high current density of 6000 mA g^{-1}). As shown in previous study, the high rate performance highly depended on the rapid ionic and electronic diffusion and transport.[16] In our case, the small size of Fe_2O_3 nanoparticles can significantly shorten the lithium ion and electron diffusion distance. The porous structure facilitates the penetration and diffusion of electrolyte, leading to fast lithium ion transport. And also, the interconnecting graphene network can provide 3D electron conducting channels within the electrode. In this way, both high speed electron and lithium ion pathways are provided. In contrast, H-Fe_2O_3/GS and pure Fe_2O_3 exhibited much poorer rate capability and cannot bear large current densities due to the inefficient ionic and electronic transport.

Besides higher capacity and better rate capability, S-Fe_2O_3/GS electrode also displayed superior cycling stability. When cycled at 500 mA g^{-1}, the capacity of pure Fe_2O_3 decayed significantly and retained only 93 mAh g^{-1} after 50 cycles (**Figure 7**a). In the case of H-Fe_2O_3/GS, though the cycling stability was greatly improved (capacity retention was 76.4%), the specific capacity can only reach 565 mAh g^{-1} after 500 cycles. Again, the capacity decay in most cases is due to the agglomeration of active materials that impair electronic and ionic diffusion. Here, the capacity decay issue was prominently resolved in S-Fe_2O_3/GS electrode, which preserved a capacity as high as 850 mAh g^{-1} after 500 cycles, maintaining 86.6% of the initial capacity. To further demonstrate the extraordinary cyclic stability of S-Fe_2O_3/GS, the electrode was tested at a higher current density of 2000 mA g^{-1} with larger numbers of cycles (Figure 7b). It showed the stabilization of the reversible capacity to 830 mAh g^{-1} after 20 cycles and good cycling performance thereafter: a capacity as high as 733 mAh g^{-1} was still retained over 1000 cycles. The capacity decay was as low as 0.027% per cycle, exhibiting an excellent prolonged cycling stability. The average coulombic efficiency was nearly 100% from the second cycle, indicating stabilization of SEI.[40] To the best of our knowledge, this is one of the best Fe_2O_3/GS anodes reported to date in terms of high rate performance and cycle life.

To explore the material stability, which is directly related to battery cyclic stability, we further investigated the structure and morphology of the cycled electrodes by TEM. As shown in Figure 7c, the Fe_2O_3 particles grew slightly to 30–60 nm due to the formation of SEI layer.[32,33] However, the particles still possessed the initial shapes, showing their good structure robustness. The primary dispersibility was also well preserved, demonstrating a good constraint on the aggregation of Fe_2O_3 upon cycling. The persistent uniform distribution of Fe_2O_3 as well as its excellent structural robustness should contribute the most to the extraordinary cycling stability. The magnified TEM image revealed an amorphous nature of Fe_2O_3 after battery cycling (Figure 7d). This suggests that the first reaction between Fe_2O_3 and lithium is not totally reversible, thus resulting in the first evolution of gel-polymer layer and the initial capacity loss.

DOI: 10.1002/smll.201303371

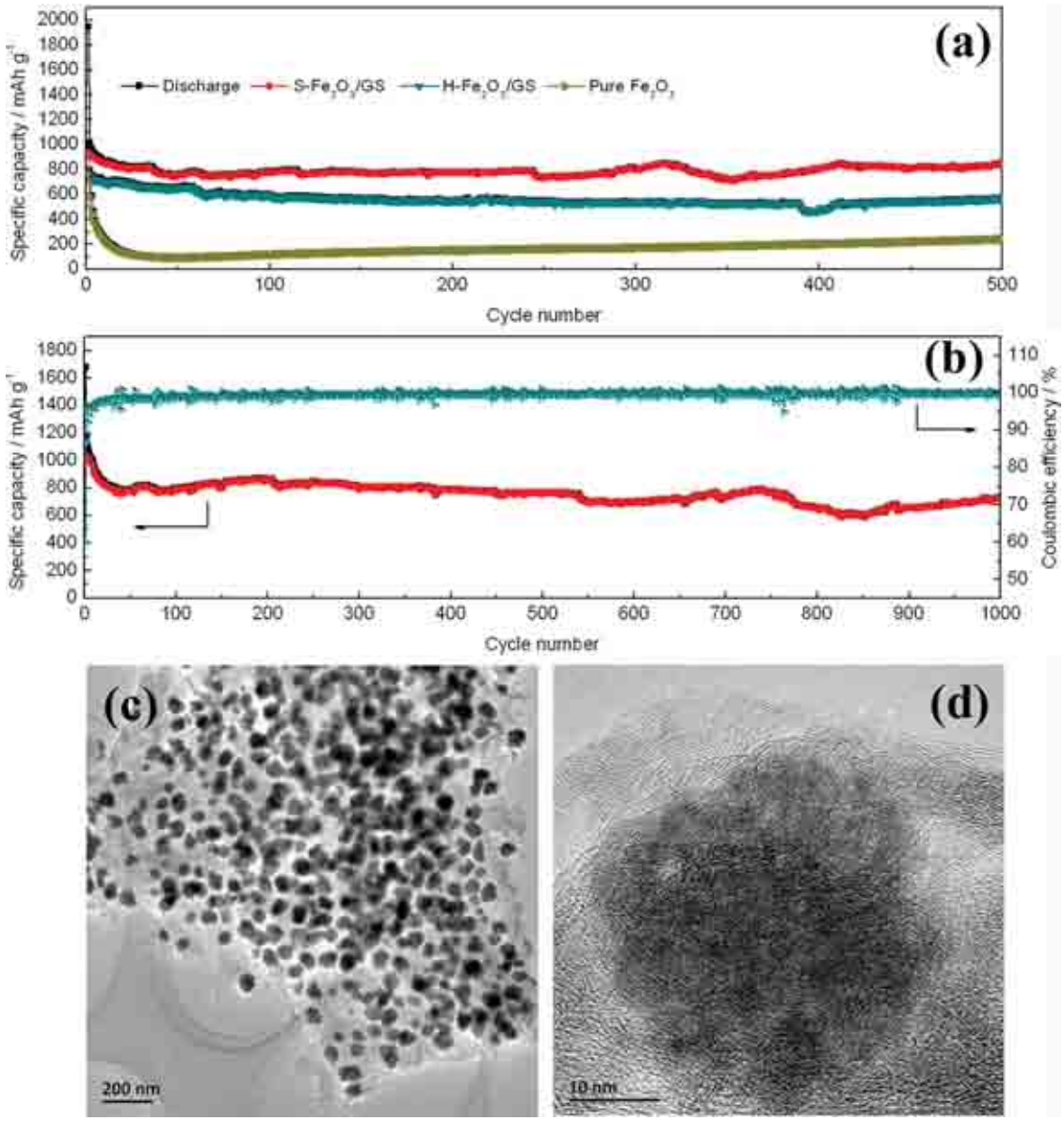

Figure 7. (a) Comparative cycle performance of S-Fe_2O_3/GS, H-Fe_2O_3/GS and pure Fe_2O_3 electrodes at a current density of 500 mA g^{-1}, (b) cycle performance of S-Fe_2O_3/GS at a current density of 2000 mA g^{-1}, (c-d) TEM images of S-Fe_2O_3/GS after cycling at 500 mA g^{-1}.

3. Conclusion

We have successfully constructed Fe_2O_3/GS aerogels via a novel solvothermal-induced self-assembly process, using $Fe(OH)_3$ sol as precursor. Solvothermal treatment restricts the growth up of Fe_2O_3 particles, enables a thorough reduction of GS, and induces formation of robust hydrogels; while $Fe(OH)_3$ sol leads to an even distribution of the final Fe_2O_3, and assists the self-assembly process. Upon cycling, the initial excellent dispersion of Fe_2O_3 particles was preserved in a robust manner, which substantially improved the cycle life. A high specific capacity of 733 mAh g^{-1} was preserved over 1000 cycles at 2000 mA g^{-1}, which are 10 times larger than those of typical battery materials. The superior rate capability, 520 and 370 mAh g^{-1} at 4000 and 6000 mAh g^{-1}, respectively, was attributed to the porous structure and 3D conductive graphene network. This versatile approach can be extended to the synthesis of the composite structures of other metal oxides to improve their potential use in numerous electrochemical and catalytic applications.

4. Experimental Section

Preparation of $Fe(OH)_3$ Sol: $Fe(OH)_3$ sol was prepared according to our previous work.[33] $FeCl_3$ was dissolved in H_2O (5 mL) to get $FeCl_3$ solution, which was then dropped into boiling distilled water (50 mL). The solution was kept boiling for several minutes to obtain $Fe(OH)_3$ sol.

Preparation of Fe_2O_3/GS Aerogels: GO was prepared from graphite powder by the modified Hummers method.[41] In a typical synthesis, $Fe(OH)_3$ sol was added dropwise into GO dispersion (40 mL, 2 mg mL^{-1}), followed by ultrasonicating for 30 min. The

small 2014,
DOI: 10.1002/smll.201303371

mixed suspension was centrifuged and re-dispersed in DMF (40 mL) to form $Fe(OH)_3$/GO dispersion and further solvothermally treated at 180 °C for 12 h. Finally, the 3D black monolith was taken out, washed repeatedly with distilled water, and freeze-dried into an aerogel for further use. The sample was named as S-Fe_2O_3/GS. As a control, $Fe(OH)_3$/GO suspension in 40 mL H_2O was hydrothermally treated at 180 °C for 12 h (the weight ratio of $Fe(OH)_3$ to GO was the same with S-Fe_2O_3/GS). The sample was noted as H-Fe_2O_3/GS. Pure Fe_2O_3 particles without RGO were also prepared by solvothermal treating of $Fe(OH)_3$ sol in DMF via a similar procedure.

Electrode Preparation: The electrodes were prepared by mixing 80 wt% active material, 10 wt% conducting carbon black, and 10 wt% polyvinylidene fluoride binder in N-methyl-2-pyrrolidone. The homogeneous slurries were then pasted on copper current collector and dried under vacuum at 110 °C for 12 h.

Material Characterization: The morphology was characterized by transmission electron microscope (JEM-2100F, JEOL, Tokyo, Japan). The field-emission scanning electron microscope (FE-SEM) analysis was performed on JSM-6700F at an acceleration voltage of 10.0 kV. X-ray diffraction (XRD) was carried out on D/max 2550V X-ray diffraction-meter with Cu-Kα irradiation at λ = 1.5406. Thermal gravimetric analysis (TGA) was conducted in the air at a heating rate of 10 °C/min. X-ray photoelectron spectroscopy (XPS) analysis was conducted using twin anode gun, Mg Kα (1253.6 eV) (Microlab 310F Scanning Auger Microprobe, VG SCIENTIFIC LTD). Conductivity was measured by a four-point probe method in the van der Pauw configuration with an Accent HL5500 system. N_2 adsorption/desorption isotherms were determined using a Micromeritics ASAP2010 Analyzer (USA).

Electrochemical Measurements: Cyclic voltammetry (CV) was carried out in a voltage range of 0–3.0 V with a scan rate of 0.5 mV s^{-1}. The electrochemical properties of the electrodes were characterized at room temperature. Li foil was used as the counter electrode. The electrolyte was 1 M $LiPF_6$ in a 50:50 w/w mixture of ethylene carbonate (EC) and dimethyl carbonate (DMC). Cell assembly was carried out in glove box with the concentrations of moisture and oxygen below 1 ppm. The batteries were measured using a CT2001 battery tester.

Supporting Information

Supporting Information is available from the Wiley Online Library or from the author.

Acknowledgements

This work is supported by the 973 Project (2012CB932303), the National Natural Science Foundation of China (Grant No. 51172261).

[1] Y. G. Guo, X. Zhou, L. J. Wan, *Chem. Commun.* **2013**, *49*, 1838.
[2] J. Sun, R. H. Wang, C. H. Xu, Y. Q. Liu, L. Gao, C. C. Lin, *Nanoscale* **2013**, *5*, 6960.
[3] R. S. Ruoff, X. J. Zhu, Y. W. Zhu, S. Murali, M. D. Stollers, *Acs Nano* **2011**, *5*, 3333.
[4] C. H. Xu, J. Sun, L. Gao, *Nanoscale* **2012**, *4*, 5425.
[5] X. Gu, L. Chen, Z. C. Ju, H. Y. Xu, J. Yang, Y. T. Qian, *Adv. Funct. Mater.* **2013**, *23*, 4049.
[6] R. H. Wang, C. H. Xu, J. Sun, L. Gao, C. C. Lin, *J. Mater. Chem. A* **2013**, *1*, 1794.
[7] J. X. Zhu, D. Yang, X. H. Rui, D. H. Sim, H. Yu, H. E. Hoster, P. M. Ajayan, Q. Y. Yan, *Small* **2013**, *9*, 3390.
[8] T. Hu, X. Sun, H. T. Sun, M. P. Yu, F. Y. Lu, C. S. Liu, J. Lian, *Carbon* **2013**, *51*, 322.
[9] a) I. T. Kim, A. Magasinski, K. Jacob, G. Yushin, R. Tannenbaum, *Carbon* **2013**, *52*, 56; b) X. Duan, L. Mei, J. Ma, Q. Li, T. Wang, W. Zheng, *Chem. Commun.* **2012**, *48*, 12204.
[10] Y. Zhao, J. X. Li, Y. H. Ding, L. H. Guan, *Chem. Commun.* **2011**, *47*, 7416.
[11] a) X. Jia, J.-J. Chen, J.-H. Xu, Y.-N. Shi, Y.-Z. Fan, M.-S. Zheng, Q. F. Dong, *Chem. Commun.* **2012**, *48*, 7410; b) J. Y. Zhong, C. B. Cao, Y. Y. Liu, Y. A. Li, W. S. Khan, *Chem. Commun.* **2010**, *46*, 3869; c) L. Zhang, H. B. Wu, S. Madhavi, H. H. Hng, X. W. Lou, *J. Am. Chem. Soc.* **2012**, *134*, 17388.
[12] Q. Y. Yan, J. X. Zhu, Z. Y. Yin, D. Yang, T. Sun, H. Yu, H. E. Hoster, H. H. Hng, H. Zhang, *Energy & Environ. Sci.* **2013**, *6*, 987.
[13] a) S. L. Chou, J. Z. Wang, D. Wexler, K. Konstantinov, C. Zhong, H. K. Liu, S. X. Dou, *J. Mater. Chem.* **2010**, *20*, 2092; b) B. Jang, M. Park, O. B. Chae, S. Park, Y. Kim, S. M. Oh, Y. Piao, T. Hyeon, *J. Am. Chem. Soc.* **2012**, *134*, 15010.
[14] A. Brandt, A. Balducci, *J. Power Sources* **2013**, *230*, 44.
[15] a) H. P. Cong, X. C. Ren, P. Wang, S. H. Yu, *ACS Nano* **2012**, *6*, 2693; b) X. H. Cao, Y. M. Shi, W. H. Shi, X. H. Rui, Q. Y. Yan, J. Kong, H. Zhang, *Small* **2013**, *9*, 3433.
[16] M. Zhang, B. H. Qu, D. N. Lei, Y. J. Chen, X. Z. Yu, L. B. Chen, Q. H. Li, Y. G. Wang, T. H. Wang, *J. Mater. Chem.* **2012**, *22*, 3868.
[17] R. G. Mendes, A. Bachmatiuk, A. A. El-Gendy, S. Melkhanova, R. Klingeler, B. Büchner, M. H. Rümmeli, *J. Phys. Chem. C* **2012**, *116*, 23749.
[18] a) Z. S. Wu, Y. Sun, Y. Z. Tan, S. B. Yang, X. L. Feng, K. Müllen, *J. Am. Chem. Soc.* **2012**, *134*, 19532; b) S. Y. Yin, Z. Q. Niu, X. D. Chen, *Small* **2012**, *8*, 2458.
[19] L. Xiao, D. Wu, S. Han, Y. Huang, S. Li, M. He, F. Zhang, X. Feng, *ACS Appl. Mater. Interfaces* **2013**, *5*, 3764.
[20] W. F. Chen, S. R. Li, C. H. Chen, L. F. Yan, *Adv. Mater.* **2011**, *23*, 5679.
[21] W. F. Chen, L. F. Yan, *Nanoscale* **2011**, *3*, 3132.
[22] Z. S. Wu, S. B. Yang, Y. Sun, K. Parvez, X. L. Feng, K. Mullen, *J. Am. Chem. Soc.* **2012**, *134*, 9082.
[23] Y. J. Gong, S. B. Yang, Z. Liu, L. L. Ma, R. Vajtai, P. M. Ajayan, *Adv. Mater.* **2013**, *25*, 3979.
[24] L. L. Tian, Q. C. Zhuang, J. Li, C. Wu, Y. L. Shi, S. G. Sun, *Electrochim. Acta* **2012**, *65*, 153.
[25] W. Wei, S. Yang, H. Zhou, I. Lieberwirth, X. Feng, K. Müllen, *Adv. Mater.* **2013**, DOI: 10.1002/adma.201300445.
[26] H. Zhang, A. J. Xie, C. P. Wang, H. S. Wang, Y. H. Shen, X. Y. Tian, *J. Mater. Chem. A* **2013**, *1*, 8547.
[27] Z. Zhang, F. Xiao, Y. Guo, S. Wang, Y. Liu, *ACS Appl. Mater. & Interfaces* **2013**, *5*, 2227.
[28] H. P. Cong, X. C. Ren, P. Wang, S. H. Yu, *ACS Nano* **2012**, *6*, 2693.
[29] N. Kang, J. H. Park, J. Choi, J. Jin, J. Chun, I. G. Jung, J. Jeong, J.-G. Park, S. M. Lee, H. J. Kim, S. U. Son, *Angew. Chem. Int. Ed.* **2012**, *51*, 6626.
[30] R. H. Wang, Y. Wang, C. H. Xu, J. Sun, L. Gao, *Rsc Adv.* **2013**, *3*, 1194.
[31] Y. Xu, K. Sheng, C. Li, G. Shi, *ACS Nano* **2010**, *4*, 4324.
[32] S. H. Lee, S.-H. Yu, J. E. Lee, A. Jin, D. J. Lee, N. Lee, H. Jo, K. Shin, T.-Y. Ahn, Y.-W. Kim, H. Choe, Y.-E. Sung, T. Hyeon, *Nano Lett.* **2013**, *13*, 4249.
[33] M. Du, C. H. Xu, J. Sun, L. Gao, *J. Mater. Chem. A* **2013**, *1*, 7154.
[34] C. F. Zhang, Z. X. Chen, Z. P. Guo, X. W. Lou, *Energy Environ. Sci.* **2013**, *6*, 974.

[35] F. Han, D. Li, W. C. Li, C. Lei, Q. Sun, A. H. Lu, *Adv. Funct. Mater.* **2012**, *23*, 1692.
[36] C. T. Cherian, J. Sundaramurthy, M. Kalaivani, P. Ragupathy, P. S. Kumar, V, Thavasi, M. V. Reddy, C. H. Sow, S. G. Mhaisalkar, S. Ramakrishna, B. V. R. Chowdari, *J. Mater. Chem.* **2012**, *22*, 12198.
[37] D. Z. Chen, H. Y. Quan, L. Jun Fei, G. Lin, *Nanoscale* **2013**, *5*, 9684.
[38] X. L. Jia, Z. Chen, X. Cui, Y. T. Peng, X. L. Wang, G. Wang, F. Wei, Y. F. Lu, *ACS Nano* **2012**, *6*, 9911.
[39] a) G. M. Zhou, D. W. Wang, P. X. Hou, W. S. Li, N. Li, C. Liu, F. Li, H. M. Cheng, *J. Mater. Chem.* **2012**, *22*, 17942; b) X. D. Xu, R. G. Cao, S. Jeong, J. Cho, *Nano Lett.* **2012**, *12*, 4988; c) D. N. Lei, M. Zhang, B. H. Qu, L. B. Chen, Y. G. Wang, E. D. Zhang, Z. Xu, Q. H. Li, T. H. Wang, *Nanoscale* **2012**, *4*, 3422.
[40] Y. Chen, B. H. Song, M. Li, L. Lu, J. M. Xue, *Adv. Funct. Mater.* **2013**, DOI: 10.1002/adfm.201300872.
[41] W. S. Hummers, R. E. Offeman, *J. Am. Chem. Soc.* **1958**, *80*, 1339.

Received: October 28, 2013
Revised: December 2, 2013
Published online: